together with high resolution TEM (HRTEM) yield information about the sample's morphology, the structure at and near interfaces, the density of defects in the crystal lattice, etc.. Scanning electron microscopy (SEM) reveals the morphology of a sample, and together with energy or wavelength dispersive X-ray analysis of the diffracted beam (EDX or WDX) the stoichiometry of the material. Electron energy loss spectroscopy (EELS) and fluorescence (XRF) techniques are utilized to determine the stoichiometry of the sample. Surface analytical methods correspond to an analysis of near surface composition by secondary ion mass spectroscopy and Auger electron microscopy (SIMS and AES), and binding energy (XPS).

The most commonly used high-resolution surface analysis technique besides SEM is the scanning probe microscopy (SPM). Here, a sharp tip scans the surface of the sample. The interaction between surface and tip depends on the characteristic physical properties of the surface which should be analysed. Since the mid 1980s, a large family of SPM related techniques, based on various types of interactions between the tip and the sample, have been developed. Different SPM techniques such as atomic force microscopy (AFM), electrostatic force microscopy (EFM), magnetic force microscopy (MFM), scanning capacitance microscopy (SCM), near-field scanning optical microscopy (NSOM) and others were proved to be capable of measuring the local physical properties of materials with nanoscale resolution. Currently, SPM is established for nanoscale characterisation of materials by using mechanical, electrical, magnetic, optic and chemical interactions between the probing tip and the surface. In addition it has been demonstrated that the SPM approach allows manipulation of single atoms or molecules and the contacting of single grain electronic devices.

Acknowledgements

The editor gratefully acknowledges Susanne Hoffmann-Eifert (FZ Jülich) for writing Section 4 and Ralf Liedtke (RWTH Aachen) for writing Section 2 as well as assisting in the compilation. Furthermore, the editor would like to thank Garsten Kügeler (RWTH Aachen) for technical assistance and Dennis Bräuhaus (RWTH Aachen) for corrections.

References

[1] C. Y. Chang and S. M. Sze, *ULSI Technology*, McGraw-Hill Int. Editions, 1996.
[2] S. Wolf and R. N. Tauber, *Silicon Processing for the VLSI*, (Vol. 1), Lattice Press, 2001.
[3] J. F. Wakerly, *Digital Design*, 3rd edition, Prentice Hall, 2001.
[4] B. Doyle et al., Intel Technology Journal, **6**, no. 2, 42 (2002).
[5] Y.-K. Choi, T.-J. King, and C. Hu, IEEE Trans. Electron Devices, **49**, 436 (2002).
[6] W. Steinhögl, G. Schindler, G. Steinlesberger, and M. Engelhardt, Phys. Rev. B **66**, 075414 (2002).
[7] J. R. Heath, 3rd International Conference on Trends in Nanotechnology (TNT), Santiago de Gompostela, Spain, Sep. 9-13, 2002.
[8] J. P. Spatz, S. Mössmer, C. Hartmann, M. Möller, T. Herzog, M. Krieger, H.-G. Boyen, P. Ziemann, and B. Kabius, Langmuir, **16**, 407 (2000).
[9] J. P. Spatz, V. Z.-H. Chan, S. Mössmer, and M. Möller, Advanced Materials (in press).
[10] S. Facsko, T. Dekorsy, C. Koerdt, C. Trappe, H. Kurz, A. Vogt, and H. L. Hartnagel, Science, **285**, 1551 (1999).
[11] K. L. Wang, J. L. Liu, and G. Jin, J. Grystal Growth, 1892, 237 (2002).
[12] O. G. Schmidt and K. Eberl, IEEE Trans. Electron Devices, **48**, 1175 (2001).
[13] O. G. Schmidt, Spektrum der Wissenschaft, no. 4, 8 (2002).
[14] B. H. Hong, S. C. Bae, C.-W. Lee, S. Jeong, K. S. Kim, Science, **294**, 348 (2001).

Film Deposition Methods

Peter Ehrhart, *Department IFF, Research Center Jülich, Germany*

Contents

8

Film Deposition Methods

1 Introduction

The deposition of thin-film functional layers on different substrates is an essential step in many fields of modern high technology, and applications range from large-area optical coatings on architectural structures to tribological layers, high-temperature superconductors, and finally to applications in micro- and nanoelectronics. Considering this broad spectrum of applications it is obvious that there cannot be one perfect deposition method which can be applied in all fields. In contrast, there is a wide spectrum of methods all on a high level of development and it is sometimes difficult to make the optimum choice. Even within the special field of information technology films of very different materials have to be considered: semiconductors, metals, especially magnetic layers, dielectric and ferroelectric oxides and organic layers. The deposition methods are dominated by depositions from the vapour phase and we will concentrate on the basic principles of these methods. A selection of vapour deposition methods is summarized in Table 1 with the generally accepted subdivision into physical and chemical methods. Physical methods may be characterized by a locally well-defined particle source and generally a free flight in vacuum to the substrate. For chemical methods, the so-called precursor molecules fill the reactor vessel as a vapour, dissociate at the hot substrate surface and release the atoms of interest. Some basic characteristics of the methods are summarized, however, the characterization is sometimes not very specific as the parameters depend strongly on the properties of the material of actual interest. Hence, there are many such comparisons in the literature showing some dependence on the personal bias of the author. A short introduction to depositions from solution is included in Sec. 4: i.e. chemical solution deposition (CSD) and the Langmuir-Blodgett method for monomolecular organic films. Of course, the list is not complete and we must refer to the literature for additional methods like electroplating (galvanic deposition) or thermal spray techniques.

	Physical Vapor Deposition			Chemical Vapor Deposition
	Evaporation / MBE	**Sputtering**	**PLD**	**CVD / MOCVD**
Mechanism of production of depositing species	Thermal energy	Momentum transfer	Thermal energy	Chemical reaction
Deposition rate	High, up to 750,000 Å/min	Low, except for pure metals	Moderate	Moderate Up to 2,500 Å/min
Deposition species	Atoms and ions	Atoms and ions	Atoms, ions and clusters	precursor molecules dissociate into atoms
Energy of deposited species	Low 0.1 to 0.5 eV	Can be high 1-100 eV	Low to high	Low; Can be high with plasma-aid
Throwing power a) Complex shaped object	Poor, line of sight	Nonuniform thickness	Poor	Good
b) Into blind hole	Poor	Poor	Poor	Limited
Scalable to wafer size	up to large	up to large	limited	up to large

Table 1: Some Characteristics of Vapour Deposition Processes (modified after Bunshah [1]).

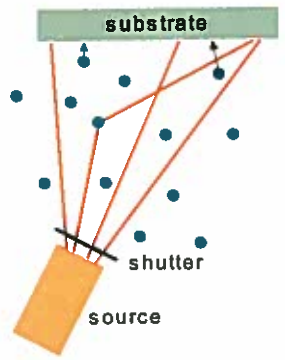

Figure 1: Schematics of a deposition system.

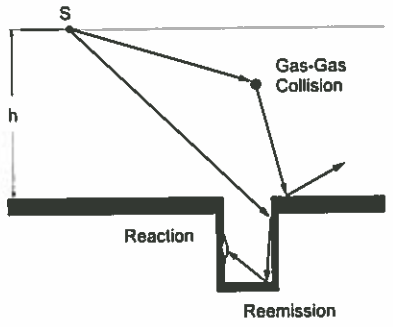

Figure 2: Deposition into a hole (after ref. 20). The example of an atom with starting position, S, with a height, h, above the substrate illustrates that either gas-gas collisions or reflection from the surface are necessary for a uniform deposition on bottom and sidewalls of a hole.

2 Fundamentals of Film Deposition

In this section, we introduce some fundamentals of film deposition which are valid for all methods. We start with the kinetics of gases as the residual gas pressure in the system determines the free path length of the deposited species and the possible incorporation of foreign atoms. Next, we discuss some basic thermodynamic data, like **vapour pressure** and **phase diagrams**, and their dependence on the residual gas pressure. Finally, we introduce the basic models for the nucleation and growth of thin films and the accommodation and release of lattice strain.

2.1 Gas Kinetics

The residual gas pressure in the system is one of the basic parameters to be controlled during film deposition as the residual gas atoms may collide with the depositing species or may hit the growing surfaces and may thus be incorporated in the film, Figure 1. For the simplest assumption that the gas atoms may be considered as not interacting masses with a Maxwell velocity distribution we obtain the mean free path length, λ, of the atoms or molecules

$$\lambda = \frac{1}{\sqrt{2}\pi N d^2} \tag{1}$$

d = molecular diameter, N = concentration of the gas. With the law of the ideal gas: $N = p/k_B T$, k_B = Boltzmann constant, we obtain:

$$\lambda = \frac{k_B T}{\sqrt{2}\pi p d^2} \tag{2}$$

For the example of air molecules we obtain a free path length which is of the order of a typical distance from source to substrate of about 20 cm at a pressure of $0.5 \cdot 10^{-3}$ mbar. This rather moderate vacuum level shows that the beam interaction is not a critical condition for the base vacuum. More critical is the number of residual gas atoms which hit the growing surface and limit the purity of the film if they are incorporated. This number can be expressed as

$$N_i = p_i \sqrt{\frac{1}{2\pi k_B m_i T}} \tag{3}$$

m_i = atomic or molecular mass. Typical results are summarized in Tab. 2. Assuming a sticking coefficient of unity, the incorporation of residual gas atoms may be expressed in terms of monolayers and this growth rate may be rather high as compared to a typical growth rate of an epitaxial film i.e., one monolayer / s. Hence, for clean films **ultra-high vacuum** (UHV, better than 10^{-9} mbar) may be necessary.

A further aspect where the mean free path of the molecules becomes important is deposition into very small structures like small via or trenches, as they are becoming more and more important with increasing miniaturization of ICs, Figure 2. Comparing the dimensions of such submicron structures with the free path lengths of Table 2 we see that even for medium vacuum conditions the mean free path of the molecules becomes much larger than the structure size. Hence, for these conditions there is no gas collision within the holes, and for the distribution of the atoms reflection at the surfaces becomes important. For simulations of the deposition processes continuum gas dynamics must be supplemented by Monte Carlo methods.

p, mbar	Mean free path, cm (between collisions)	Collisions / s (between molecules)	Molecules/(cm² s) (sticking surface)	Monolayer / s*
10^{0}	$6.8 \cdot 10^{-3}$	$6.7 \cdot 10^{6}$	$2.8 \cdot 10^{20}$	$3.3 \cdot 10^{5}$
10^{-3}	$6.8 \cdot 10^{0}$	$6.7 \cdot 10^{3}$	$2.8 \cdot 10^{17}$	$3.3 \cdot 10^{2}$
10^{-6}	$6.8 \cdot 10^{3}$	$6.7 \cdot 10^{0}$	$2.8 \cdot 10^{14}$	$3.3 \cdot 10^{-1}$
10^{-9}	$6.8 \cdot 10^{6}$	$6.7 \cdot 10^{-3}$	$2.8 \cdot 10^{11}$	$3.3 \cdot 10^{-4}$

* Assuming the condensation coefficient is unity

Table 2: Some facts about residual air at 25 °C in a typical vacuum used for film deposition (after Chopra [2]).

2.2 Thermodynamics

Phase-diagrams are the starting point for considering the deposition of a new material in order to see the stability range of the envisaged phase and the existence of concurrent phases. Standard phase diagrams are given at ambient pressure, however, changes with pressure must be considered for vacuum deposition methods. Figure 3 shows as a simple example the phase diagram of the completely intermixing binary system Si-Ge and the change from ambient pressure down to the UHV region [3]. At 1 mbar there is not much change compared to atmospheric pressure and we **observe** a wide range of stability of the mixed homogeneous crystalline phase, c, of Si-Ge (the decomposition of this homogeneous phase into two crystalline phases of different stoichiometry, c'and c", at very low temperature is somewhat speculative). At higher temperatures the liquid, l, to solid (crystalline) phase transition is indicated and above 2000 K the liquid to vapour, v, transition is shown. With decreasing pressure there is a strong decrease in temperature of the l-v borderlines and even an overlap with the c-l lines. Finally, in the UHV region, 10^{-9} mbar, the liquid has disappeared and only direct sublimation, c→v, is left at temperatures around 1100 K. Hence, re-evaporation of the material under UHV conditions and high temperatures must be considered. In addition, a comparison with the deposition rates and gas pressures discussed along with Table 2 shows that the deposition of the films usually proceeds under high supersaturation, i. e. conditions far from thermodynamic equilibrium.

Vapour pressures and the related evaporation rates present another field of basic thermodynamic data, which are very useful for the control of the deposition of different compounds. Such data can be deduced from thermodynamic data tables (e.g., CODATA and JANAF) [4]. As an illustrative example we consider Pb-based perovskite oxides (such as $Pb(Zr,Ti)O_3$, PZT for short) which are the most important class of ferroelectrics for thin film applications. The deposition of these lead-based oxides is complicated by the fact that PbO is known as a very volatile oxide. Figure 4 shows the evaporation of PbO under atmospheric conditions and under UHV: under atmospheric pressure the volatile species is PbO and the vapour pressure of Pb is 3 orders of magnitude lower. In contrast, under UHV conditions the dominant species in the vapour phase is Pb.

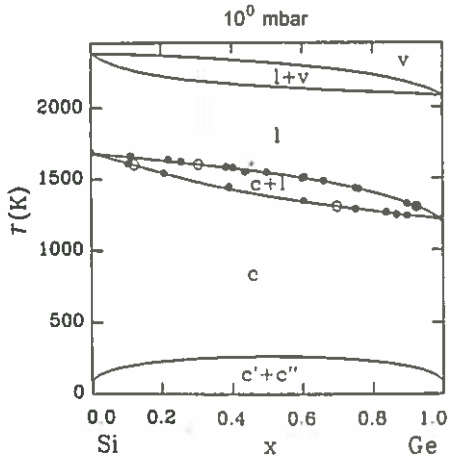

Figure 3: x–T phase diagram of the $Si_{(1-x)}$-Ge_x systems at 10^{0} and 10^{-9} mbar [3].

2.3 Film Growth Modes

Nucleation and growth of a film proceeds from energetically favourable places on a substrate surface and even the cleanest polished surface shows some structure. Figure 5 shows schematically the structure of a well-polished single-crystal surface. The charac-

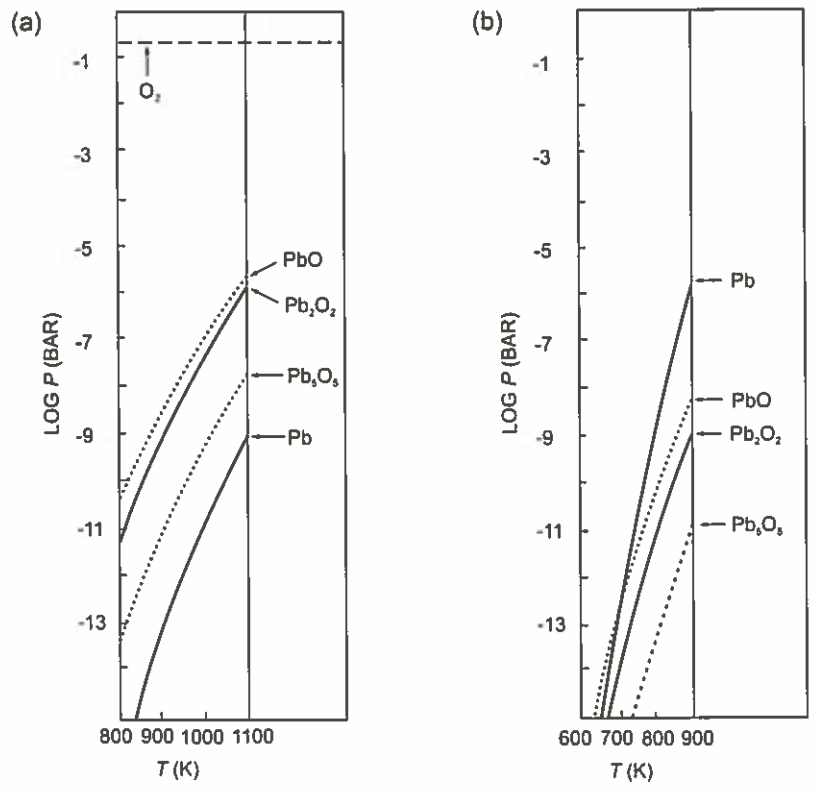

Figure 4: Vaporization of PbO at different oxygen partial pressures, (a) 0.2 bar and (b) 10^{-15} bar [4].

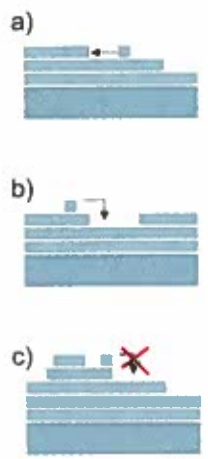

Figure 7: Growth modes of homoepitaxy: (a) step-propagation, (b) 2d-island growth, and (c) multi-layer growth.

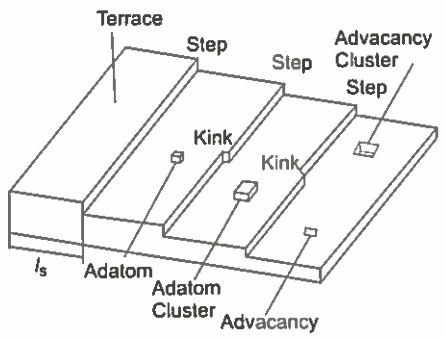

Figure 5: Schematic view of the elements of the surface morphology [3].

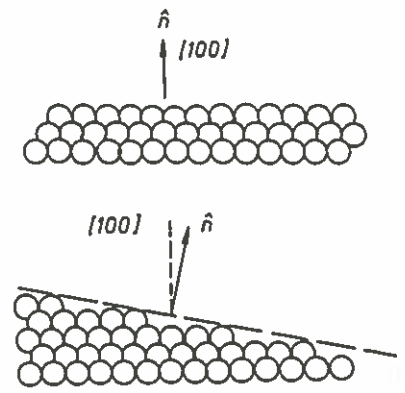

Figure 6: Change of the step distance, l_s, by cutting a surface at a small angle to a major crystallographic direction, i.e., forming a vicinal surface.

teristic features are the terraces of length, l_s, the steps and the kinks within the step line, which otherwise runs along well-defined crystallographic directions. If the surface diffusion is fast enough a randomly deposited adatom will diffuse to the energetically most favourable places like steps and especially kinks. If at lower temperatures the diffusion is slower, several mobile adatoms may encounter each other within a terrace and may form additional immobile adatom clusters within the terraces. Similarly, advacancies and their clusters might be formed at the end of the coverage of a terrace. By reducing the step distance and hence the diffusion length by vicinal surfaces, Figure 6, the step controlled growth may be extended to lower temperatures,.

The details of the growth modes for the simplest case of **homoepitaxy**, the growth of a film on a single-crystalline surface of the same material, is indicated in Figure 7. As discussed above, step propagation dominates at higher temperatures and/or small deposition rates and two-dimensional island growth will predominate if immobile clusters are formed by the encounters of mobile adatoms. This simple picture is, however, quite frequently modified: if the jump across the step is kinetically hindered multilayer growth will be observed. This enlarged activation energy for the jump across the step is called the Ehrlich-Schwoebel effect and can be understood in a simple model as the adatom is nearly dissociated from the surface in the saddle point of this jump.

If we want to grow an epitaxial film on a different substrate (so-called **heteroepitaxy**), two material parameters have to be considered in addition: the surface energy, γ, and the lattice parameter or lattice match of the two materials. For the case of good lattice match the difference in surface energy leads to two different growth modes as indicated in Figure 8a and b. As long as :

$$\gamma_{layer} + \gamma_{substrate/layer} \leq \gamma_{substrate} \tag{4}$$

we observe perfect wetting and pure layer by layer or *Frank-van-der-Merve growth*. For the opposite case, we observe island or *Volmer-Weber growth*. For this consideration the surface energies of the crystallographic orientations of actual interest must be applied, which are often not available in data reference tables. If there is a lattice mismatch between substrate and film, an additional growth mode may be observed as indicated in Figure 8c, *Stranski-Krastanov growth*. A first layer may grow matched to the substrate, which yields additional strain energy. With growing thickness this strain energy increases in proportion to the strained volume and an island formation may become more favourable in spite of the larger surface area.

The contributions of strain and surface energy can quite generally be described in a simple model and the resulting difference in energy between island growth and layer growth is given by Eq. (5) and illustrated in Figure 9.

$$\Delta W = W_{surf} + W_{relax} = const_1 \gamma d^2 - const_2 k \xi^2 d^3 \tag{5}$$

k = bulk modulus, ξ = strain

Considering films of the same volume content, the increased surface energy for the island growth Figure 8b, is proportional to the island area, d^2 , whereas the energy released by relaxation of the lattice is proportional to the island volume, d^3. A relaxation

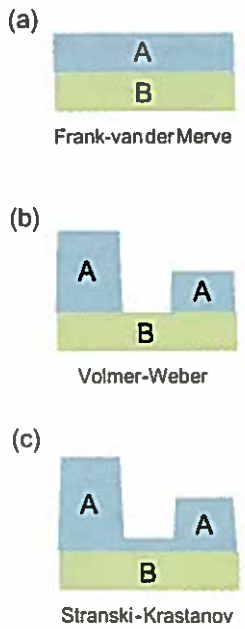

Figure 8: Growth modes of the hetero-epitaxy.

mode which is characteristic of isolated islands is shown in Figure 10 for a case where the film material has a larger bulk lattice parameter than the substrate. The model predicts a critical value, d_{crit}, where the island growth is finally more favourable and a fast decrease of the energy for larger sizes. However, the limits of the model are reached in this region as the simple relaxation mode is obviously no longer valid for large sizes.

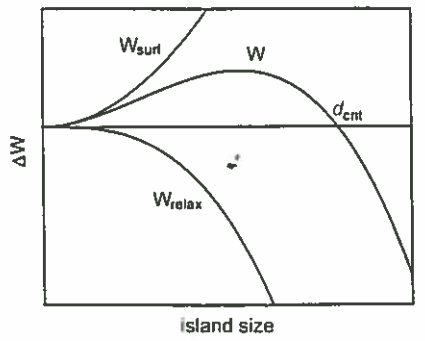

Figure 9: Energy contributions as a function of the island size [5].

2.4 Strain Relaxation in Continuous Films

Along with film growth, the islands will overlap and a closed film will form, which can no longer relax by the mechanism discussed above. A possible mechanism for strain relaxation is the formation of **misfit dislocations** as schematically shown in Figure 11. As long as the film is rather thin, there is perfect epitaxy on the substrate, however, the unit cell is tetragonally distorted; as the in-plane lattice parameter is forced to smaller values, an expansion, according to Poisson's ratio, is observed in the direction perpendicular to the film. This tetragonal structure is manifested by the different in-plane and out-of-plane lattice parameters and by a tilt of the crystallographic angles, e.g., a deviation of the [110] direction from 45 °. This strain is relaxed by the formation of dislocations as indicated in Figure 11b, and the film returns, in principle, to the cubic structure, however, the interface is only semi-coherent.

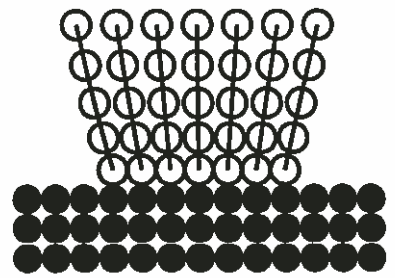

Figure 10: Strain relaxation in pseudomorphic (dislocation - free) islands.

3 Physical Deposition Methods

In this Section, we will give a short introduction to the basic principles of the different physical deposition methods and some comments on their advantages and drawbacks. Some special features of the different techniques will be demonstrated by examples which are selected to additionally demonstrate the wide field of thin-film applications in microelectronics and the wide spectrum of analytical tools for the characterization of thin films.

3.1 Thermal Evaporation / Molecular Beam Epitaxy

Molecular beam epitaxy (MBE) has evolved from simple thermal evaporation techniques by the application of UHV techniques to avoid disturbances by residual gases, and additionally includes many different sources. A schematic view of a system is shown in Figure 12 including several different sources which allow the controlled deposition of multi-element compounds. The main components and their use are summarized in Table 3: these are the different beam sources, the shutters, which are very important for controlling the growth of dopant profiles or multi-layers, the process environment and, very specific for MBE, the in-situ process control. Due to the UHV environment all UHV surface techniques might be applied, but only reflection high energy electron diffraction (RHEED) is included here as an example.

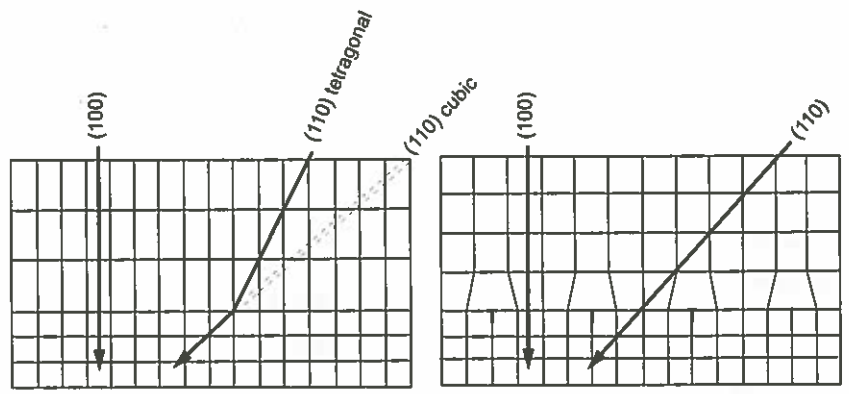

Figure 11: Strain relaxation by misfit dislocations for the example of two initially cubic crystals. As the film has a larger lattice constant than the substrate the forced matching at the interface yields a tetragonal distortion of the film. By misfit dislocations this strain can be relaxed and the film can re-approach its cubic structure.

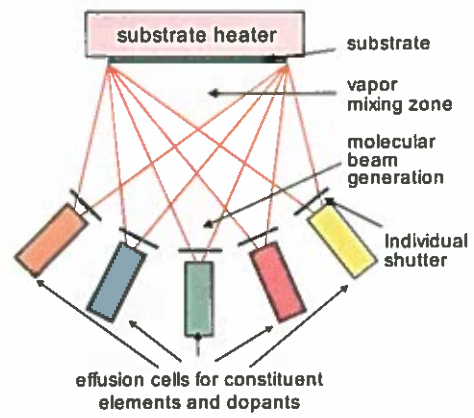

Figure 12: Schematic view of a MBE system for the growth of multi-element compound films.

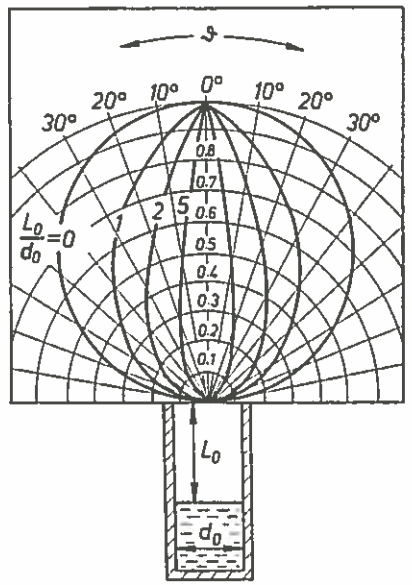

Figure 13: Schematics of a Knudsen cell and the distribution of the vapour beam intensity [7]. The distribution depends on the ratio L_0/d_0 and consequently on the filling level of the cell.

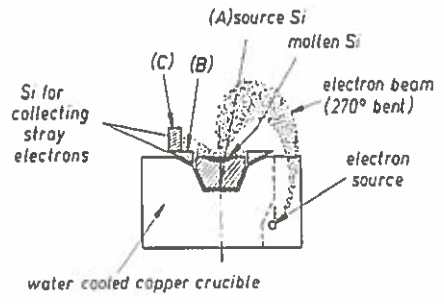

Figure 14: Schematics of a electron beam evaporator for Si evaporation [7]; B: Si guard ring, C: catcher for backscattered electrons.

Facilities	Components	Functions
Beam generators	Knudsen cells e^- - beam evaporators Gas or vapour cells	To provide stable, high-purity, atomic or molecular beams impinging onto substrate surface ⇒ MOMBE
Beam interruptors	Fast-action shutters	To completely close or open line of sight between source and substrate. Action should be rapid (< 0.1 s) and should cause minimal thermal disruption of source
Process environment	Multichamber UHV system	To provide ultraclean growth environment, with residual gas species (e.g. O_2,CO, H_2O,CO_2) $< 10^{-11}$ mbar
Beam and growth monitors	RHEED Beam monitoring ionization gauge mass spectrometer	To provide dynamic information on the surface structure on beam intensities and on compositional information

Table 3: Principle operative systems in MBE and their function (after Parker [6]).

3.1.1 Sources

The schematic of the classical MBE source, the Knudsen cell, is illustrated in Figure 13. The evaporation rate, N_e, is described by the Hertz-Knudsen (or Langmuir) equation:

$$N_e = \frac{p_e A_e}{\sqrt{2\pi m k_B T}} \qquad (6)$$

p_e is the equilibrium vapour pressure and A_e the area of the aperture [7]. Therefore, the source can be precisely controlled by a single parameter, the temperature. However, the technical details are very complex and involve more parameters than shown in Eq. (6) .

Figure 14 shows the principle of an electron beam evaporator. The electron beam is magnetically deflected by 270° and is centred on the source material. In this way a melt of the source material is produced on a block of the same material which can be held in a water-cooled cold crucible in order to avoid contamination of the melt.

3.1.2 Process Environment

Larger MBE systems are composed of modular stainless steel building blocks and Figure 15 gives an example: the deposition chamber, the wafer or substrate preparation chamber and often an additional analytical chamber. All operative components are attached by flanges for service access. All materials used within the system need special consideration in terms of low gas desorption and high resistance to heating during out-gasing at elevated temperatures. Parts with high heat load are liquid-nitrogen-cooled ('cryo panel') . Pumping systems include turbomolecular pumps, especially in parts with larger gas load, cryopumps and ion getter pumps.

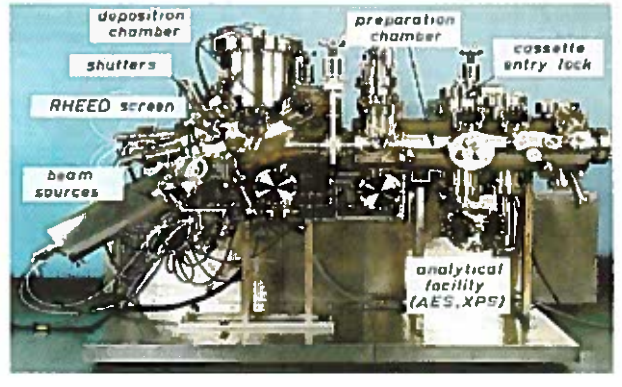

Figure 15: Overview of an MBE system [7].

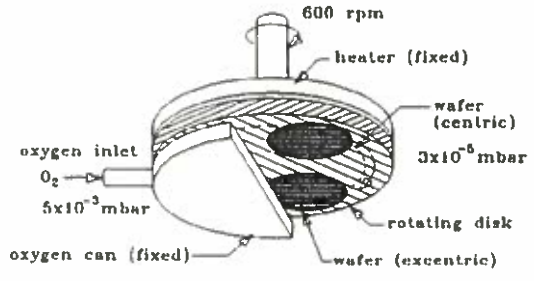

Figure 16: Control of the oxygen partial pressure by differential pumping [8].

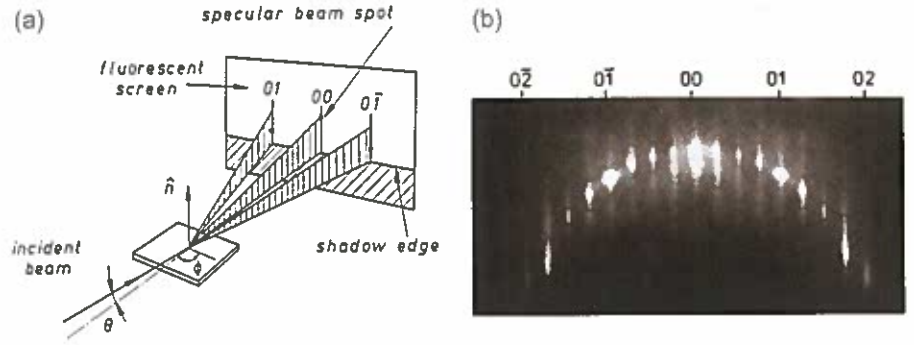

Figure 17:
(a) Schematics of the RHEED geometry; the elongated diffraction spots indicate the cut of the Ewald sphere with the 01 , 00, and 0-1 reflections of the quasi-two-dimensional lattice,
(b) diffraction pattern of a reconstructed GaAs (001)-(2x4) surface [7].

The oxygen partial pressure for the deposition of some oxide films is a major problem for the UHV technique. However, several solutions have been used including differential pumping as indicated in Figure 16, i.e. by rotation of the substrate the film is temporarily exposed to oxygen whereas the sources and the vapour are under high vacuum conditions in order to avoid oxidation and deterioration of the sources [8].

3.1.3 In-situ Analytical Techniques

One of the decisive advantages of MBE is the possibility of implementing all UHV surface analytical techniques and controlling the growth process in situ. We will shortly introduce RHEED as a simple method which is most widely used . Figure 17a shows the schematic set-up. An electron beam of typically 10 keV hits the film under a flat angle and is reflected yielding a specular spot as well as diffracted spots. Figure 17b shows an example of the diffraction pattern of a GaAs surface.

The intensities of the diffraction spots yield detailed information on the surface structure, however, for monitoring the growth it is sufficient to monitor the intensity of the specular spot as shown in Figure 18. At the beginning of deposition there is a very flat substrate and a strong specular spot; with increasing coverage, θ, the intensity decreases and for coverage larger than $\theta = 0.5$ it increases again. Generally, the coverage of 1 is not exactly reached again as adatoms and vacancies accumulate during growth and yield a slightly larger roughness. Nevertheless, every individual layer can be controlled by the observed oscillations. In the example shown there are some slower oscillations after closing the shutter which indicate a re-evaporation under the given conditions as discussed in Section 2.2. RHEED shows, of course, only the changes and cannot distinguish between growth and re-evaporation

3.1.4 Example: Epitaxial Growth of Fe Films

Figure 19 gives an example of the application of MBE techniques for the deposition of metallic films as will be discussed in the lectures on magnetic layers. Fe-Cr layers are model systems for the investigation of magnetic exchange coupling and the figure shows a study of the growth of Fe layers. Perfect single crystalline substrates are available in the form of whiskers with step length in the order of 1 µm. The change of the film growth as a function of the deposition temperature is illustrated and the development of a process window for the deposition is indicated [9]. At room temperature we observe a fast decay of the amplitude of the oscillations, which indicates an increasing surface roughness along with the film growth, and this roughness is established by the scanning tunneling microscope, STM. There is a steady improvement with temperature and a perfect layer growth can be observed at 250 °C where the surface diffusion seems fast enough to allow perfect layer by layer growth.

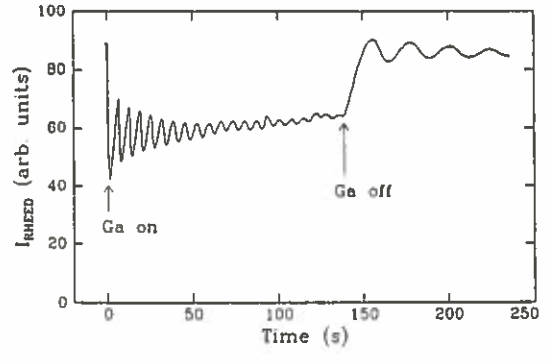

Figure 18: Growth and re-evaporation of GaAs as observed by RHEED [3].

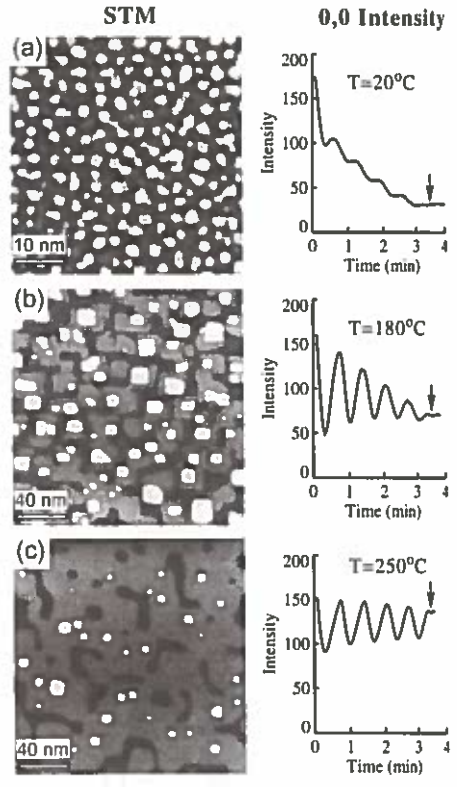

Figure 19: STM and RHEED results for the homo-epitaxial growth of Fe films on Fe(100) substrates. The growth was interrupted after 5 oscillations, as indicated by the arrow. The scale of the STM was changed between part a and b! The roughness of the films decreases strongly with temperature: rms (root mean square) amplitude 0.116 nm , 0.095 nm and finally at 250°C 0.06 nm [9].

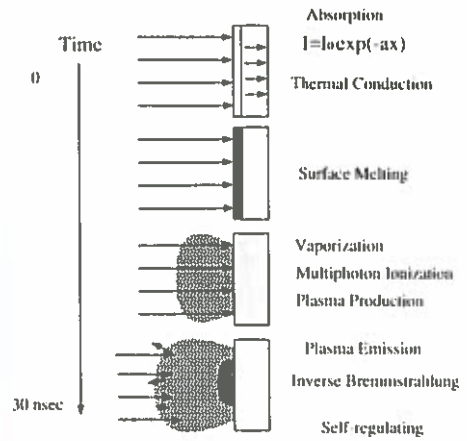

Figure 20: Set-up of a pulsed laser deposition system for the deposition of oxide layers.

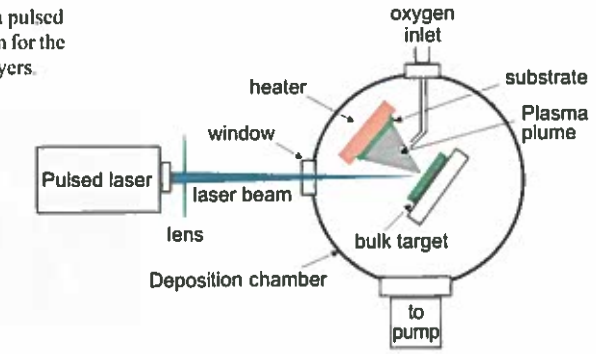

Figure 21: Time evolution of the plasma plume [10].

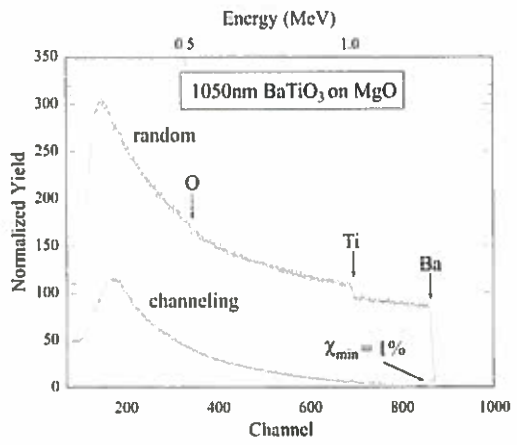

Figure 22: RBS/Channelling measurement of a $BaTiO_3$ thin film on MgO(100) [13].

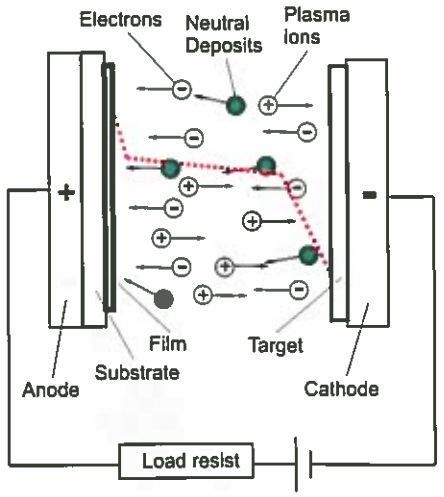

Figure 23: Schematics of a DC-sputter system, the red dotted line indicates the potential between anode and cathode.

3.2 Pulsed Laser Deposition

3.2.1 PLD Concept

The concept of a PLD experiment is basically simple and is shown in Figure 20. A short pulsed laser beam from an excimer laser is focused onto a target. The pulse energy of typically 1 J/pulse leads to the immediate formation of a plasma due to the high energy density of 3-5 J/cm^2 at the target surface. The plasma contains energetic neutral atoms, ions and molecules and reaches the substrate surface with a broad energy distribution of 0.1 to > 10 eV. Details of the laser ablation process [10] are summarized in Figure 21. A problem of the method is that, in addition to the energetic neutral atoms, ions and molecules, some small droplets may be deposited on the film ending up as so-called 'boulders'. Different methods have been developed to reduce these effects, e.g. time-of-flight selection of the deposits [11] as the heavier particles are slower, or the use of an off-axis geometry [12]. In off-axis PLD geometry the surface of the substrate is placed parallel to the expansion direction of the plasma. This geometry has the additional advantage that samples larger than the lateral extension of the plasma plume can be used, however, only if the target is rotated in order to obtain a homogeneous film.

Based on the extensive work on high-temperature superconductors the deposition of oxide films is well developed. Very satisfactory photon absorption within the oxide target is provided at UV wavelengths and characteristic deposition parameters are: wavelength of the laser beam of 248 nm or 193 nm and a repetition rate ≈ 50 Hz at a pulse length of 25 ns. For the growth of epitaxial oxide thin films sufficient ion mobility is needed. It is provided by a substrate temperature typically exceeding 750 °C, which is provided e.g. by an oxygen-resistant SiC heater. An ambient oxygen pressure of 0.3 to 1 mbar may be maintained within the chamber.

3.2.2 Example: Optical Waveguides

Electro-optical thin films made of $LiNbO_3$, $KNbO_3$ and $BaTiO_3$ (BTO) with thickness of the order of microns were prepared using the pulsed laser deposition technique [13]. The deposition temperature and the oxygen pressure during the growth process are used to control the crystalline perfection, the orientation and the grain size of the film. As a typical example, a single crystalline thin BTO film on MgO(100) is shown in Figure 22. An RBS analysis is performed to characterize these BTO films. The RBS analysis provides information about the stoichiometry and the homogeneity. In connection with ion channelling measurements additional information is obtained about the crystal perfection of the investigated material. The RBS-channelling analysis shows the correct stoichiometry of the BTO film with a minimum yield of 1 %, which proves the single crystalline growth of BTO on MgO(100). Such a 1 µm thick $BaTiO_3$ film prepared on MgO(100) forms a waveguide showing optical losses as low as 3 dB/cm, which is an excellent result for such thin electro-optical BTO films.

3.3 Sputter Deposition

Sputtering of surface atoms has been known since 1852 when W.R. Grove observed this effect during his investigations of plasma discharges and it was soon recognized that this sputtering can be applied for the deposition of thin films. However, the large-scale technological application only developed during the last few decades (see e.g., [14], [15], [16] for review).

3.3.1 DC Sputtering

The simplest sputtering approach is so-called DC sputtering, which is schematically shown in Figure 23. In a vacuum chamber the target material, which is eroded, is at the cathode side (negative potential), and the substrate for the film is at the opposite anode side. The potential of several 100 volts between these plates leads to the ignition of a **plasma discharge** for typical pressures of 10^{-1}-10^{-3} mbar and the positively charged ions are accelerated to the target. These accelerated particles sputter off the deposits, which arrive at the substrate mostly as neutral atoms. The discharge is maintained as the accelerated electrons continuously ionize new ions by collisions with the sputter gas. The potential distribution between anode and cathode is indicated by the dotted red line: as the plasma is a good conductor there is no major potential drop in the plasma region, and due to the different mobility of electrons and ions the main voltage drop is observed at the cathode (darkroom). This potential distribution is advantageous as the acceleration of the sputtering gas ions proceeds directly in front of the target and not in a region far off, where the ions would undergo additional collisions and lose their energy on the long path to the target.

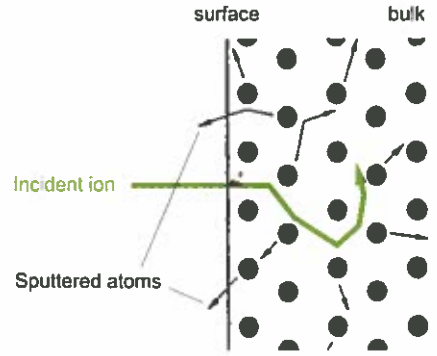

Figure 24: Principle of the sputtering of surface atoms by a collision sequence after the incident ion has hit the target surface [14].

3.3.2 Sputtering Process

The sputtering process is schematically illustrated in Figure 24. The ion, which has been accelerated within the darkroom with nearly the full voltage applied of 50 to 1000 eV, hits the surface atoms. The following **collision cascade** leads to a heating of the target and finally also to some back-reflected atoms which can leave the surface. The details of these collision cascades can be simulated very reliably by 'molecular dynamics' methods, and basically depend on the relative masses of projectile and target atom. Some results of the sputtering yield for incident Ar ions on different target materials are shown in Figure 25 [14]. The threshold energy for sputtering is much higher than the surface binding energy, W_b, of the atoms which is of the order of 4 to 8 eV. This difference can be directly understood as several collisions are necessary in order to obtain an atom in the backward direction. Hence, the threshold is observed at $4W_b$ to $8W_b$ corresponding to a threshold energy of 20 to 50 eV. A linear increase is observed for many conditions up to voltages of 1000 eV. At higher energies the ions penetrate too deeply into the target and the yield decreases again. As shown in Figure 25, different sputtering yields are observed for different target atoms and this difference in principle yields the deposition of a film of different stoichiometry. However, there is generally a good self-regulating mechanism: due to the very low penetration depth of the sputtering process the component eroded faster is denuded after a short initial time and finally in a quasi-equilibrium the difference in yield is compensated by the enrichment. Therefore, sputtering quite generally allows the deposition of films with the same stoichiometry as the target.

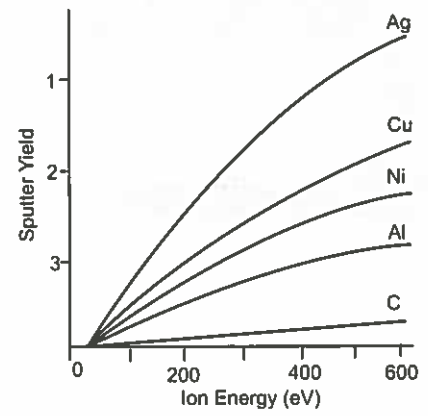

Figure 25: Dependence of the sputtering yield on the energy of the incident Ar ions and of the target properties [14].

3.3.3 Magnetron Sputtering

An ionization degree of less than 1% of the atoms is characteristic of a plasma and consequently a rather low sputter rate. To improve the ionization rate magnetic fields can be used which force the electron onto helical paths close to the cathode and yield a much higher ionization probability [10], [14]. This magnetron arrangement additionally allows a lower gas pressure, however, it has the disadvantage of more inhomogeneous target erosion than a simple planar geometry.

3.3.4 RF Sputtering

DC sputtering works very well as long as the target material shows some electrical conductivity. For insulating targets, however, a high-frequency plasma discharge, as shown in Figure 26, must be applied in order to avoid the accumulation of electric load. A typical frequency of 13.6 MHz is capacitively coupled to the target and there is only a small voltage decay across the electrode. As the electrons are much faster than the ions a negative potential at the electrodes as compared to the plasma potential evolves during each cycle. With a symmetrical arrangement of cathode and anode we would obtain similar re-sputtering rates and no film growth, however, non-symmetries, which yield some bias voltage, are introduced by the coupling of the RF and by differences in the geometry, i.e., different sizes of target and substrate, and especially by the generally applied grounding of the substrate and the deposition chamber. Nevertheless, deposition rates are much lower than for DC sputtering.

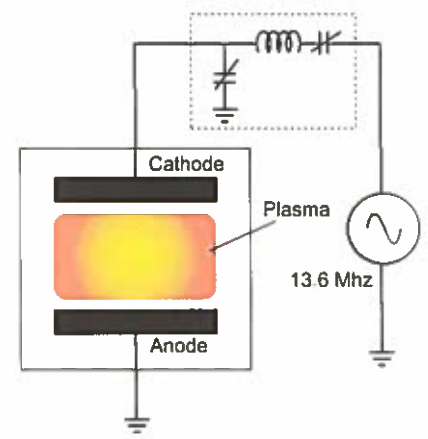

Figure 26: RF-plasma sputter system with RF matching network [14].

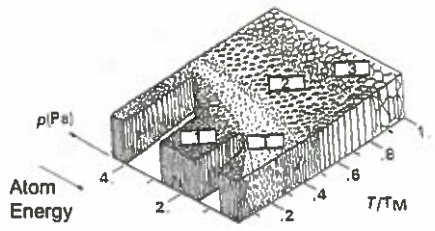

Figure 27: Structure zone diagram for sputter-deposited metals after Thornton [17].

Figure 28: DC-sputter deposition in 'high pressure' oxygen.

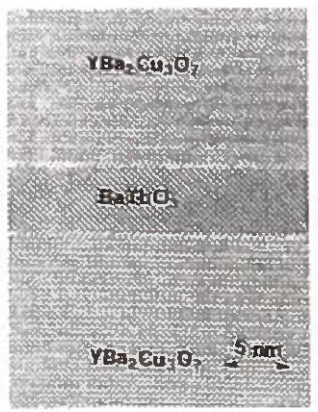

Figure 29: HRTEM micrograph of a sputter deposited trilayer system [19].

3.3.5 Gas Pressure and Film Growth

Compared to the other physical deposition methods the partial pressure of the sputtering gas is an additional and important process parameter which must be considered and optimized. This pressure controls the free path length of the atoms and therefore their energy, angular distribution and finally also their incorporation in the film. For metals, so-called zone diagrams for the film growth have been developed [17], which show some systematic dependencies on the normalized temperature (the substrate temperature, T_s, normalized by the melting temperature, T_m) and the pressure, Figure 27.

Zone 1: $T_s < 0.2\ T_m$: at these low temperatures no bulk diffusion and only very limited surface diffusion is observed which would allow for crystallite rearrangement. Grain structure is composed of fibres whose size and orientation are determined by the initial random nucleation of the grains. Some shielding effects are visible depending on the angle of deposit incidence. This structure extends to higher temperatures, when the ion energy is reduced due to gas collisions. The size of the fibres increases with temperature mainly following the temperature dependence of the nucleation density.

Zone T: $(0.2 - 0.3\ T_m)$: In this transition zone, surface diffusion becomes effective and small crystals of energetically unfavourable orientation are eliminated, i.e. a competitive texture is observed.

Zone 2 and 3: $T_s > 0.5\ T_m$: Evolution of morphology and texture is determined by reconstruction, single crystalline columns are formed with increasing diameter, and, finally, texture is determined by the lowest free energy surface of the crystal. The influence of the Ar pressure decreases.

For oxide layers the gas pressure is even more important as negative oxygen ions are formed which can re-sputter from the film. As the re-sputtering yield also depends on the different elements the stoichiometry of the growing film is changed and these changes of the film are not compensated as was the case for the sputter yield from the target discussed above. This re-sputtering can be reduced by so-called high pressure oxygen sputtering [18] where the energy of the ions is reduced by the increased number of gas collisions connected to the shorter free path length; however, it must be considered that this high gas pressure also reduces the deposition rate.

3.3.6 Example: High Pressure Oxygen Sputtering

Figure 28 shows a high-pressure, a few mbar, oxygen sputtering system which is operated in DC mode for the given example of the deposition of electrically conducting oxide films [19]. Perfect control of the interface and epitaxial growth can be obtained by this 'low energy' sputtering process at rather slow growth rates. These perfect interfaces are demonstrated by the cross-sectional HRTEM view of the resulting multilayer structure, Figure 29, which is used as a junction barrier in high T_c devices [19].

4 Chemical Deposition Methods

Chemical deposition generally includes **chemical solution deposition** (CSD) as well as **chemical vapour deposition** (CVD). In both cases, chemical precursors are employed which undergo chemical reactions for the formation of the film. We will place special emphasis on CVD as this method finally allows the deposition of ultrathin films and the conformal deposition on complex-shaped structures which are essential for ULSI. CSD includes sol-gel techniques and metal-organic decomposition MOD and typically uses spin-on techniques for the distribution of a solute film which is subsequently processed and crystallized. Finally, we give a short introduction to a very different method for deposition from solutions, the **Langmuir-Blodgett** (LB) technique. LB techniques allow the deposition of monomolecular organic films on different substrates making use of the hydrophilic/hydrophobic orientation of the molecules.

4.1 Chemical Vapour Deposition

The general principles of CVD are well established and a number of reviews and textbooks are available [20], [21], [22], which cover many generic issues common to any type of material. In CVD, film growth occurs through the chemical reaction of the component chemicals (i.e. precursors) which are transported to the vicinity of the substrate via the vapour phase. The film-forming chemical reactions typically utilize thermal

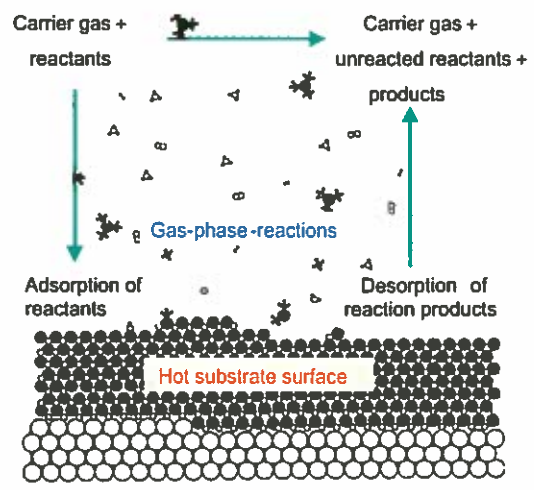

Figure 30: Schematics of the gas flow and the atomic scale chemical environment in the region of the growing film surface during a MOCVD process.

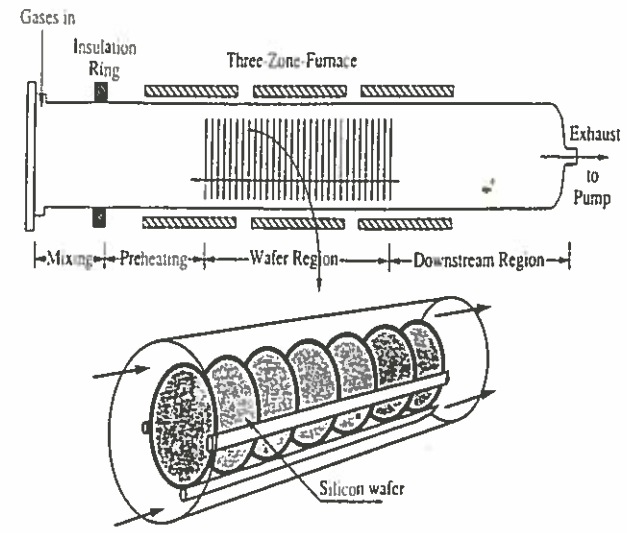

Figure 31: Schematic representation of a hot-wall multiple-wafer in-tube CVD reactor [20].

energy from a heated substrate as depicted schematically in Figure 30. Other more special methods, which cannot be discussed here, couple non-thermal energy sources such as RF or microwave power or light into the reaction process in order to reduce the thermal reaction temperature required. In order to complete the system, a delivery system for the precursors and, finally, an exhaust system must be added. The most straightforward type of CVD involves chemical precursor compounds that are sufficiently stable gases and such processes are standard processes in CMOS technology for the deposition of insulators and interlayer dielectrics like poly-Si, SiO_2, SiN_x and BPSG glasses. Figure 31 shows the schematics of a reactor for handling large batches of wafers simultaneously. Examples of the reactions involved are the thermal decomposition of silane, SiH_4, for the deposition of:

- Poly Si : $SiH_4 \rightleftharpoons Si(s) + 2\ H_2$ at 580-650 °C, and a pressure of ≈ 1 mbar;
- Si-Nitride: $3\ SiH_4 + 4\ NH_3 \rightleftharpoons Si_3N_4 + 12\ H_2$ at 700-900 °C, and atmospheric pressure;
- Si-Dioxide: $SiH_4 + O_2 \rightleftharpoons SiO_2 + 2\ H_2$ at 450 °C;

These SiO_2 films are usually under high stress and are not conformal. Therefore alternative routes using organic precursors have been developed e.g., the TEOS (tetra-ethyl-ortho-silane) process:

$$Si(C_2H_5O)_4 + 12\ O_2 \rightleftharpoons SiO_2 + 8\ CO_2 + 10\ H_2O \text{ at } 700\ °C.$$

Similarly, for the processing of many metals and especially the group-II metals, special precursors in the form of organometallic compounds had to be developed and a special subgroup of CVD techniques, **metal-organic**-CVD, MOCVD, has therefore evolved. Efficient, reproducible MOCVD processes hinge critically upon precursors with high and stable vapour pressures and the chemistry is therefore the decisive step in the development of MOCVD.

4.1.1 Precursor Chemistry and Delivery

Only a sufficiently high vapour pressure enables vapour-phase mixing of precursor components and transport of the reactants to the growing film and a vapour pressure of > 0.1 mbar at 100 °C is considered to be a lower limit. Adequate molecular stability of the precursor vapour is required to prevent premature reaction or decomposition of the precursor during vapour phase transport; these requirements characterize a process window between vaporization and decomposition of the precursor. Additional requirements

β-Diketonates

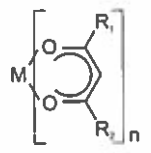

$R_1=R_2=CH_3$ (acetylacetonate)
$R_1=R_2=C(CH_3)_3$ (tetramethylheptadionate) ····· **Ba(thd)$_2$, Sr(thd)$_2$**
$R_1=C(CH_3)_3$, $R_2=CF_3$ (trifluorodimethylhexanedionate)
$R_1=C(CH_3)_3$, $R_2=C_3F_7$ (heptafluorodimethyloctanedionate)
$R_1=R_2=CF_3$ (hexafluoroacetylacetonate)

Organometallics

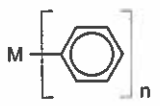

phenyl

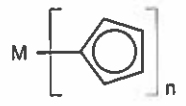

cyclopentadienide

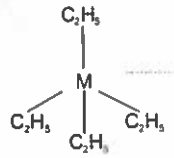

tetraethyl

tetra-ethyl-**lead**

triphenyl-**Bi**

Alkoxides

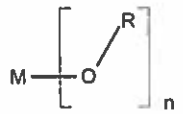

$R=CH_3$ (methoxide)
$R=C_2H_5$ (ethoxide)
$R=CH(CH_3)_2$ (isopropoxide) ····· **Ti**: TIP, **Zr**: ZIP
$R=C(CH_3)_3$ (t-butoxide) ····· **Zr** -tert -butoxide

Figure 32: Selection of precursor molecules for oxide deposition [25].

are long-term stability of the precursors (e.g. low moisture sensitivity), complete decomposition (no contamination of the film e.g. by fluorine) and last but not least low toxicity and environmental regulatory requirements.

For complex oxides the precursor molecules typically contain the metal atoms, M, and organic groups, R. In most cases, such as in alkoxides, ketonates, and carboxylates, the metal atom is bound to the organic group through an oxygen atom, i.e. M-O-R. This is different from precursors used for the MOCVD of compound semiconductors where the precursors are conventional metal organic compounds, i. e. M-R systems. For heavy cations (especially group-II elements), a reasonable volatility is often reached only by organometallic precursors, e.g. by β-diketonates with several alkyl groups, such as in tetramethylheptadionates (thd) (and this type of organometallic precursor is the origin of an alternative acronym occasionally used: OMCVD). The two keto groups chelate the cation while the outer alkyl groups effectively shield any polar region of the molecule. Typically two (thd) ligands are reacted with one cation yielding $Ba(thd)_2$. Since the outer shell of this molecule consists entirely of alkyl groups there is only a weak van-der-Waals interaction between neighbouring molecules and, hence, a relatively low boiling temperature. For cations with a higher electronegativity (i.e. a lower tendency to form ionic bonds), alkyl compounds, such as $Pb(C_2H_5)_4$, and alkoxide compounds, such as $Ti(OC_3H_7)_4$, may give rise to a sufficient volatility [23].

The different types of precursors used for oxide deposition are summarized in Figure 32. The main applications for the present topics of IT are included in the figure: e.g., the diketonates for Ba and Sr, thd = tetramethylheptadionate, alkoxides for Ti (TIP = titaniumisopropoxide = $Ti(O\text{-}i\text{-}Pr)_4$) and Zr. Mixed precursors like $Ti(O\text{-}i\text{-}Pr)_2(thd)_2$ are also used to increase compatibility with other precursors. In addition, adducts or stabilizers are used in order to avoid reactions and oligomerization e.g., tetraglyme or pmdeta. Most of these precursors are liquid or solid at room temperature and reach a sufficient vapour pressure only at elevated temperature. Therefore, special delivery systems are necessary, i.e. bubblers or liquid source delivery systems.

A bubbler system as used for PZT deposition is shown in Figure 33. Three different liquid precursors are held at elevated temperature:

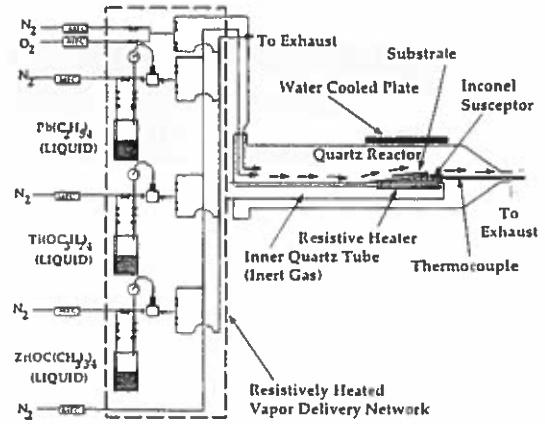

Figure 33: MOCVD research reactor with bubbler system and quartz tube horizontal flow reactor used for PZT deposition [25].

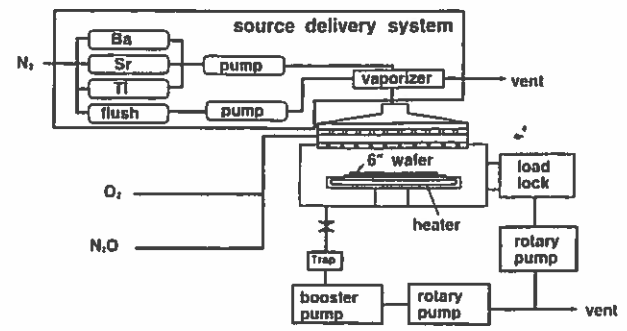

Figure 34: MOCVD production tool with liquid source delivery system showerhead reactor and load lock used for BST deposition [26].

$Pb(C_2H_5)_4$: bubbler held at 50 °C with a vapour pressure of 2 mbar
$Ti(OC_3H_7)_4$: at 95 °C and 5 mbar,
$Zr(OC_4H_9)_4$: at 65 °C and 1 mbar.

The vapour is transported by a carrier gas to the reactor where the mixing of the vapour occurs. The flow rate of the precursors, f_p, given in sccm (standard cm^3 per minute) or mol/min is:

$$f_p = \frac{f_c p_p}{p_{tot} - p_c} \tag{7}$$

the index p refers to the precursor and c to carrier gas. The partial pressure of the precursors, p_p, can be calculated from the Clausius-Clapeyron equation:

$$\frac{d(\ln p)}{dT} = \frac{\Delta H}{k_B T} \tag{8}$$

where ΔH is the enthalpy of evaporation. For stable temperatures, the flow can be controlled by the flow of the carrier gas. The lines must be held at the bubbler temperatures in order to avoid condensation.

For group-II metals the precursors are solid up to higher temperatures and the vapour pressures are even lower e.g. $Ba(thd)_2$: 0.05 mbar at 200 °C and $Sr(thd)_2$: 0.20 mbar at 230 °C. As the precursors are not very stable at these temperatures a direct sublimation is not favourable and so-called liquid delivery systems have been developed. The precursors are dissolved in an appropriate solvent, e.g., butylacetate, and evaporated in close vicinity to the reactor. Such a system is shown in Figure 34. Here the liquids are mixed and finally flash-evaporated in a vaporizer on top of the reactor. Alternative evaporation systems use aerosol-assisted nebulizers or controlled single droplet injection systems [24].

4.1.2 Reactor Design and Modelling

The reactor must provide a controlled gas flow and heat distribution and for the precursors discussed here it should work at low pressure (10^{-1} to 10 mbar) in order to keep the number of gas collisions of the molecules very low. In addition, its construction materials must withstand oxygen and other aggressive chemicals even at elevated temperatures, and typical materials are e.g. quartz, SS and coated graphite. Figure 33 shows a small-size research reactor with quartz as the structural material and a simple gas flow system [25]. Figure 34 shows a reactor design for routine deposition of large wafers [26]. The evaporated precursors are homogeneously distributed by a so-called showerhead. The pumping system consists of a roots or booster pump and a rotary pump for the pumping of larger gas loads including the carrier gas. Finally, a load lock system is shown as is necessary for routine production. In order to increase the throughput, batch processing tools have to be developed also for oxide films and first results have been reported for an AIXTRON 2600G3 Planetary Reactor®, which can handle five 6-inch wafers simultaneously [27].

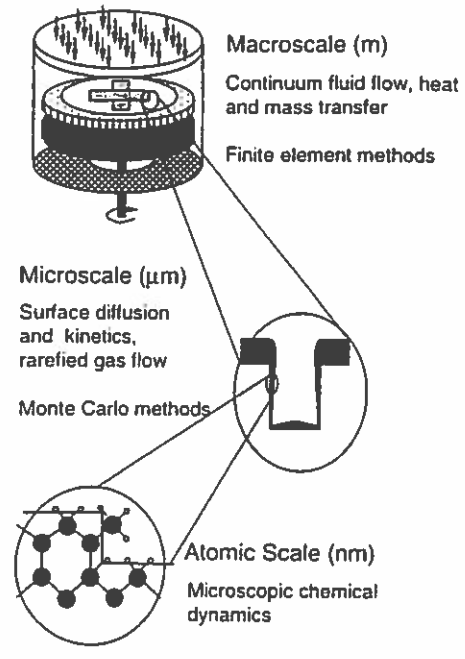

Figure 35: Schematic illustration of the coupling of micro- and macroscale phenomena in CVD processes [20].

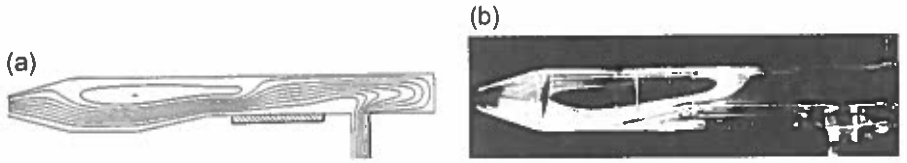

Figure 36:
(a) Calculated flow pattern in a horizontal reactor; the formation of transverse convection rolls is observed.
(b) Flow visualization with TiO_2 smoke demonstrating the existence of a transverse roll cell in the horizontal flow reactor and a dark space above the susceptor caused by thermophoretic migration of the smoke particles away from the hot susceptor [20].

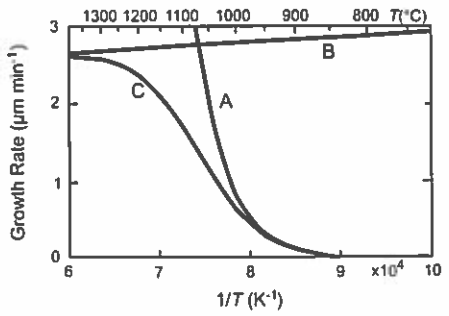

Figure 37: Schematic view of the control of the growth process: A: kinetic control, B: transport control, C: resulting behaviour; the actual temperature scale corresponds to the deposition of poly-Si from $SiCl_4$ [20].

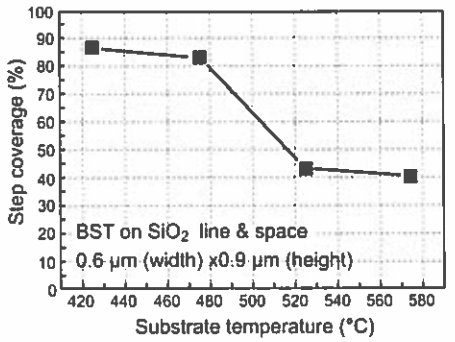

Figure 38: Dependence of the step coverage on the deposition temperature [26].

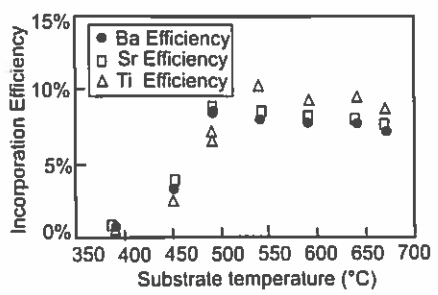

Figure 39: Dependence of the incorporation efficiency on the deposition temperature [29].

A complete understanding of the complex MOCVD process includes processes on very different length scales as indicated in Figure 35: Macroscale (turbulence, cold or hot spots), microscale (e.g., conformal deposition) and finally atomic-scale (chemical reactions, nucleation and growth, desorption). Considering the large number of design parameters, it is desirable to simulate the whole process in order to obtain an estimate of the reactor behaviour. Although complete modelling has to combine the simulation on all length scales, modelling can usually be performed separately on different scales and we restrict ourselves to some examples.

The deposition rate and the final composition of the film are primarily controlled by the spatial profiles of gas velocities and temperatures as well as of the partial pressure of the various precursors in the reactor. Collectively, these profiles are referred to as the reactor flow pattern. For CVD, a laminar gas flow pattern is generally required in order to obtain process reproducibility. The parameters which determine these profiles are either directly controllable (i.e. the total flow rates of gases the total reactor pressure, the flow rates of individual reactants, the temperature of the susceptor and occasionally the temperature of the reactor walls) or are fixed by the design of the system (i.e. the configuration of the gas injection manifold, the design of the exhaust flange, and the shape, size and materials of the deposition chamber and susceptor). For the modelling of this macroscale, the fluid flow in the reactor, the temperature gradient and the mass transfer finite element methods are widely used. By this modelling, disturbances of the laminar flow or regions of low temperatures, cold rolls, can be detected and corrected by changes of the reactor geometry. Results can be given in terms of dimensionless parameters like the Reynolds number, the Raleigh number and others, and can therefore be transferred to similar reactor types [20]. Figure 36 shows as an example the flow pattern in a horizontal flow reactor with the formation of a transverse convection cell and the experimental verification of such a cell by visualization through light scattering at TiO_2 smoke.

Although MOCVD is generally not a process under thermodynamic equilibrium conditions, the system's thermodynamic data can yield a lot of background information on phase stability assuming quasi-equilibrium phase distributions. As an example, Ref. [28] reports on the phase distribution under typical MOCVD deposition conditions for BST, and especially on the strong influence of the precursor mix on the formation of carbonate phases.

A typical example of calculations on the microscale is deposition into trenches or vias, as shown in Figure 2. It is obvious that the free path length of the gases (or the pressure) is an important parameter in this field and the optimum filling conditions for different geometrical details of the structure can be predicted, e.g., for a hole with a given aspect ratio, the ratio of the depth to the width.

4.1.3 Growth Control

Thermal energy, e.g. supplied by the heated substrate, is the primary source of energy fuelling film growth. Depending on the temperature, two different ranges for the limitation of the growth rate can be distinguished: at low temperatures the growth is usually limited by the reaction kinetics and at higher temperatures by the mass transport as shown schematically in Figure 37.

The reaction kinetics includes many different process steps ranging from precursor reactions, which may include many decomposition reaction steps, to the film growth kinetics. Hence, an effective activation energy, W_a, must generally be expected and the kinetically limited growth rate, j_k, may be written as:

$$j_k = const_1 N^{\infty} e^{-\frac{W_a}{k_B T}} \tag{9}$$

N^{∞} = precursor concentration at some distance from the substrate.

At medium and higher temperatures the exponential increase of the kinetically limited growth rate yields only a negligible limitation and the major limitations of the reaction are given by the transport of the precursors and reactants to the surface (i.e., by the diffusivity of the gases, D), and the so-called transport limited growth rate, j_t , is given by:

$$j_t = const_2 N^{\infty} \frac{\sqrt{D}}{T} \tag{10}$$

where the diffusion constant of the gas is: $D = \lambda \langle u \rangle / 3$, and $\langle u \rangle$ is the average velocity of the gas atoms. In contrast to the diffusion in the solid state, the diffusivity in gases shows only a weak temperature dependence, and consequently also j_t (Figure 37). Within the simplest ideal gas approximation this yields $j_t \propto 1/T^{1.4}$, which is in reasonable agreement with more realistic calculations that also consider the reactor geometry and yield $j_t \propto 1/T^{1.6}$. The overall growth rate, j_g, may be obtained by adding the two reciprocal fluxes, which can be considered as two resistive elements in series:

$$\frac{1}{j_g} = \frac{1}{j_k} + \frac{1}{j_t} \tag{11}$$

This means that the slower flux finally determines the growth rate. At even higher temperatures there is usually a decrease for different reasons: thermodynamics (exothermic reaction), precursor stability, pre-reactions etc. In spite of the complexity of the processes there are some general rules which may guide the selection of the appropriate temperature region (as the gas diffusivity depends on pressure, the limits depend on pressure, too).

Mass-transport–limited region: The deposition rate is insensitive to small temperature gradients and cold wall reactors are therefore often operated in this regime. However, the local deposition rate is very sensitive to the flow pattern, which may be complex for cold-wall reactors, and which is, as shown above, an indirect consequence of temperature gradients; hence uniformity problems may arise in this regime.

Kinetically limited region: The deposition rate is only weakly dependent on the flow homogeneity, therefore this regime is best suited for conformal deposition. However, the exponential temperature dependence necessitates a very high stability of the temperature as well as a good uniformity over large wafers.

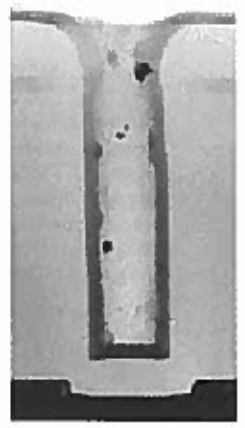

Figure 40: MOCVD of $SrTiO_3$ thin films into a test hole of a SiO_2 layer with an aspect ratio of 1:6 and a width of 150 nm. The deposition was performed in a dome-type reactor at a wafer temperature of 420°C. The TEM cross section shows the very high conformality of the thin film [30].

4.1.4 Conformal Deposition

Conformal deposition is a prerequisite for applications in ULSI, e.g. for high-K dielectrics in DRAMs. The additional requirements for conformal deposition yield a strong restriction within the process parameter field for the optimization of the film properties. Conformality is expected in the regime of kinetically controlled growth, and as discussed above low temperatures and low pressures are favourable. As demonstrated by the example of $(BaSr)TiO_3$ (BST) depositions, Figure 38, the conformality is strongly improved at lower temperatures [25], however, the incorporation rate of the precursors decreases with lower temperatures [29] as indicated in Figure 39. In addition there are some differences for different elements which strongly affect the reproducibility of the stoichiometry. Hence, for these conditions there is only a very narrow process window to achieve conformality and reasonable deposition rates simultaneously. Nevertheless, very good conformality even in narrow holes with a high aspect ratio, i.e., ratio of width to depth, of 1:6 has been achieved [30] as demonstrated in Figure 40.

4.1.5 Layer by Layer Growth and Ultrathin Films

Similar to MBE, layer by layer growth is the final goal of the development of the technique and it has been achieved for metal-organic MBE (MOMBE) as a hybrid system. Although in situ control is limited with conventional MOVCD, optical methods and ion beam analyses in differentially pumped systems have been tested, and III-V compound multilayer systems for LED and laser diodes are deposited with high perfection. Additional approaches for the control of the layer growth include pulsed organometallic beam epitaxy (POMBE) and as a specific chemical approach, **atomic layer epitaxy** (ALE) and **atomic layer deposition** (ALD) which use the chemisorption of special polar molecules [32]. This process is illustrated in Figure 41 for the example of the deposition ZnS as used for phosphorus screens. In the first step the chemisorption of the precursor molecules, $ZnCl_2$, yields a saturated monolayer on the surface of the substrate. In the subsequent step the reactant, H_2S, reacts with this adsorbate and a monolayer of ZnS is deposited without external control of the reaction time. As there is no adsorption of the reactant on ZnS the next monolayer may be deposited similarly. Such a process yields atomic layers even without epitaxial growth. The deposition of ternary systems is of course much more difficult, nevertheless the development of a process for the deposition of BST has been reported [32].

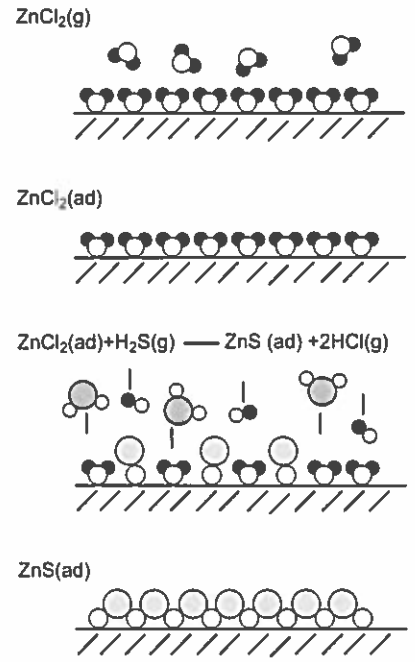

Figure 41: Principle of the ALD for the example of ZnS [31].

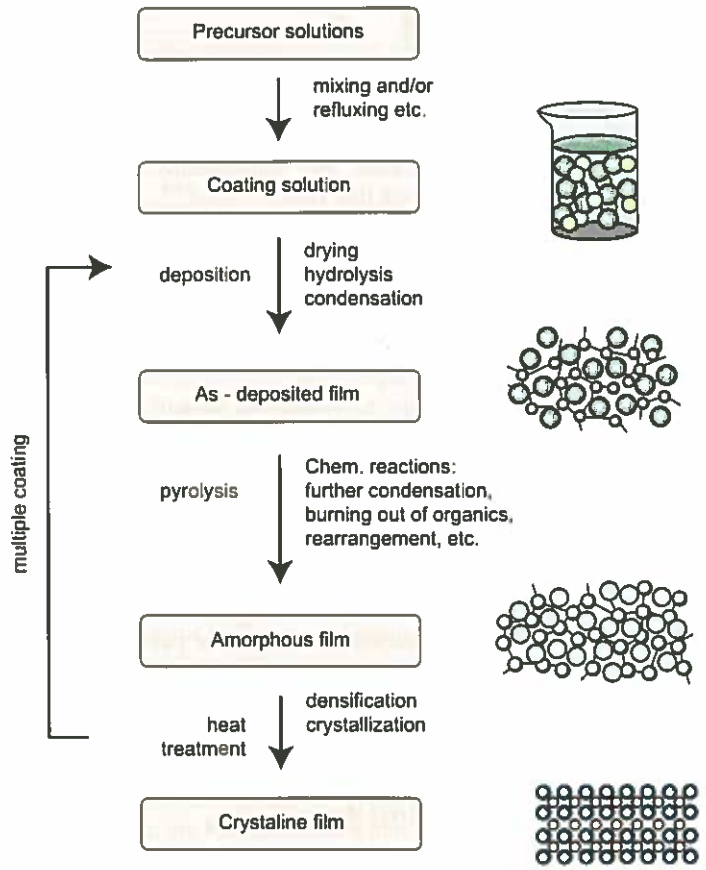

Figure 42: Flow chart of the chemical solution deposition technique. The bars describe the states during the CSD procedure, while the arrows indicate the treatment and the internal processes [23].

4.2 Chemical Solution Deposition

The chemical solution deposition (CSD) method comprises a range of deposition techniques and of chemical routes which have been reviewed recently [23], [33]. A generalized flow chart of the CSD of oxide thin films is shown in Figure 42. The process starts with the preparation of a suitable coating solution from precursors according to the designated film composition and the chemical route to be used. Besides mixing, preparation may include the addition of stabilizers, partial hydrolysis, refluxing, or else. The coating solution is then deposited onto substrates by:

- *spin-coating,* where typically a photoresist spinner is employed and which is suitable for semiconductor wafers,
- *dip coating,* which is often used in the optics industry for large or non-planar substrates, and
- *spray coating,* which is based on a misting of the coating solution and deposition of the mist exploiting gravitation or an electrostatic force.

The wet film may undergo drying, hydrolysis and condensation reactions depending on the chemical route. The as-deposited film possibly represents a chemical or physical network. Upon subsequent heat treatment, a further hydrolysis and condensation and/or a pyrolysis of organic ligands may take place, again depending on the chemical route. The resulting film consists of amorphous or nanocrystalline oxides and/or carbonates. Upon further heat treatment, any carbonate will decompose and the film will crystallize through a homogeneous or a heterogeneous nucleation. Typically, the desired final film thickness is built up by multiple coating and annealing.

Depending on the type and reactivity of the precursors, the chemistry shows a wide spectrum of reaction types. On the one hand, there are the pure sol-gel reactions i.e. alkoxide precursor systems, which undergo hydrolysis and condensation reactions. The formation of SiO_2 coatings starting from Si alkoxides is the classical example of this type of reaction. The condensation leads to a chemical gelation in which – under appropriate reaction conditions – no pyrolysis reaction of any organic ligand occurs. At the other extreme, there is **metal organic decomposition** (MOD), which typically starts

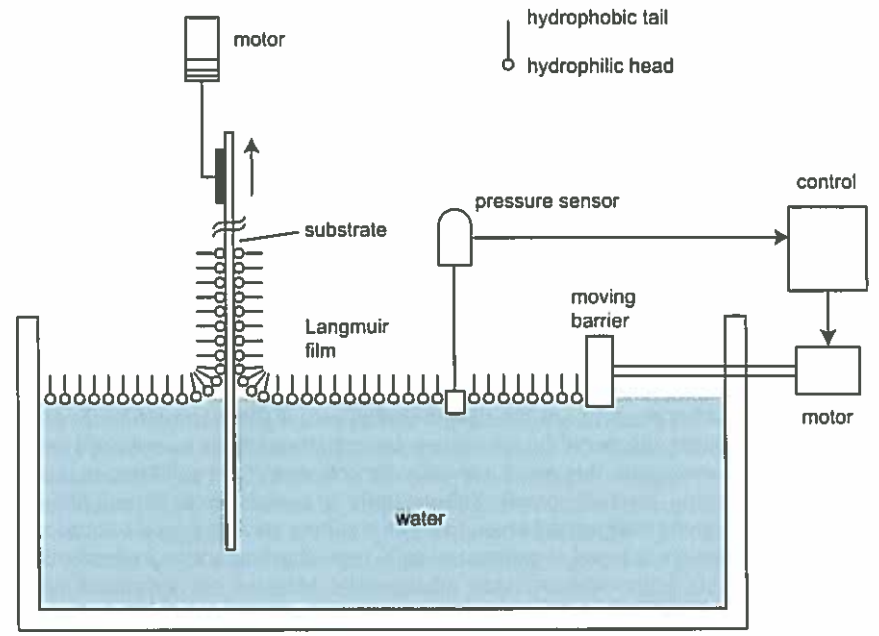

Figure 43: Trough for the controlled deposition of LB films; for details see text.

from carboxylates of the cations or, in special cases, from the nitrates. The carboxylates do not chemically react with water. Consequently, during heat treatment, first the solvents are evaporated, a process which is sometimes referred to as physical gelation. Upon further heating, the carboxylates pyrolytically decompose into amorphous or nanocrystalline oxides or carbonates. There is a wide spectrum of possible reaction routes between the pure sol-gel route and the MOD route. Depending on the type of alkoxides and a possible stabilization of the precursors, there may be a partial hydrolysis and condensation while some organic ligands remain in the gelated film and undergo pyrolysis upon further heat treatment. In the synthesis of multicomponent oxide films, often hybride routes are followed, i.e. there may be some precursors employed which tend to follow the sol-gel or partial sol-gel route while others undergo typical MOD reactions.

The microstructure formed during the CSD process strongly depends on the thermodynamics and kinetics of the solidstate reaction from the intermediate amorphous or nanocrystalline state after pyrolysis to the final equilibrium crystalline phase. This is controlled by the chemical composition of the film system (for details see e.g. ref. [23]).

Due to their low capital investment and simple processing, CSD techniques are widely used and are also applicable for micro- and nanoelectronics on a low level of integration, e.g. for present state FeRAMs.

4.3 Langmuir-Blodgett Films

Organic thin films can be deposited with all of the methods discussed above and especially CSD (spincoating) and CVD techniques are widely used for the deposition of low-K dielectrics in microelectronic integration technology [34]. With special consideration of the stability of the molecular reactions under high electronic excitation even sputter deposition [16] and PLD [12] have been considered. The aspects of heteroepitaxy of large molecules on inorganic substrates have been discussed in detail recently [35]. Organic light emitting diodes (OLED's) consisting of rather complex layer stacks have been deposited by MBE [36]. For organic molecules there is, however, an additional powerful deposition method which should be shortly introduced.

The Langmuir-Blodgett (LB) method is a classical method of surface chemistry for the deposition of molecular monolayers and multilayers and its development is closely connected with the oil on water problem. The organic molecules that are used in this type of deposition contain two types of functional groups. One end of the hydrocarbon chain is soluble in water (hydrophilic), e.g., acid or alcohol group, and the other end contains insoluble hydrocarbon groups (hydrophobic). As a result the molecules form a film on the surface of water (a Langmuir film) with the hydrophilic end at the water side.

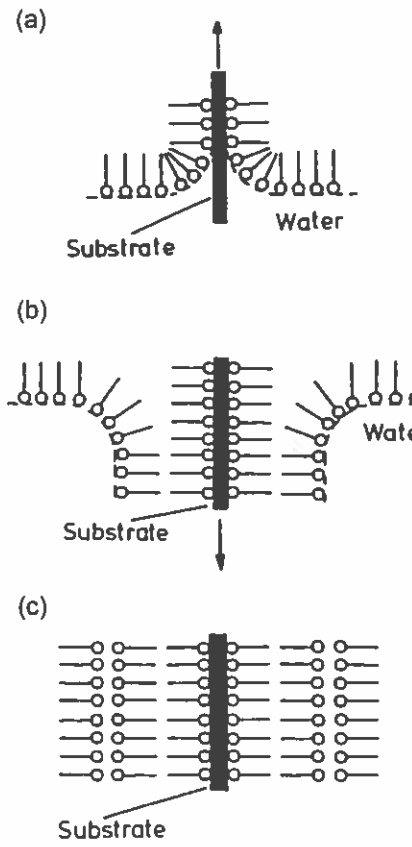

Figure 44: Y-type deposition sequence [39].

Pockels showed already in 1891 that such a film can be compressed to form a continuous monolayer on the liquid. The final step was achieved by Blodgett in 1935 when she demonstrated that the film adheres to a solid surface passing through the air-water interface.

Starting from this simple principle, remarkable technical progress has been achieved and starting in the mid-1970s fully automated troughs for building monomolecular layers and multilayers have been developed [37]-[39]. Figure 43 illustrates the basic principle: a substrate is removed from a bath which contains a monomolecular Langmuir film on a water surface. The Langmuir film is kept under a constant 2-D pressure by a moving barrier and a control unit. By this process, a monolayer of the organic molecules is transferred onto the substrate.

The details of the adsorption process and the underlying chemistry are complex and depend on many parameters, however, some basic processes can be specified. Firstly, we consider a hydrophilic substrate as shown in Figure 44: (a) The first monolayer is transferred as the substrate is raised through the subphase; if there is a strong hydrophilic interaction no layer adheres if the substrate is lowered through the compressed subphase and for weak interaction this result can only be obtained if the substrate is immersed before the floating layer is spread. Subsequently a monolayer is deposited on each traversal through the compressed layer, (b). The resulting stack is a head to head and tail to tail configuration, (c), and is referred to as Y type. Starting with a hydrophobic substrate the double layers are arranged analogously. Most of the substrates used are hydrophilic, e.g., transparent substrates like glass and quartz, metals like Al or Cr and their oxides, and also silicon wafers, which are most widely used. Care must be taken, however, in cleaning the surfaces, e.g. clean Si or oxidized Si are hydrophilic whereas a treatment with Cl (dimethyldichlorosilane) yields a hydrophobic Si surface.

So-called X- and Z-type films can be obtained if the films are deposited only during the immersion or the removal of the substrate from the liquid. In this case the interactions between adjacent monolayers are hydrophilic-hydrophobic and stable growth is most likely observed for weakly hydrophilic headgroups. Therefore these multilayers are less stable than the Y-type systems. Both X- and Z-type films are non-centrosymmetric and are therefore considered for applications in nonlinear optics. Depending on the chemistry and / or the deposition mode and speed there are also deviations from these ideal deposition modes. This different adsorption behaviour can be quantified by the ratio ϕ.

$$\phi = \frac{\theta_u}{\theta_d} \tag{12}$$

θ_u and θ_d are the deposition (or transfer) ratios on the upward and downward passages as originally defined by Langmuir comparing the area occupied by the monolayer on the water and on the substrate. Thus $\phi = 1$ corresponds to the ideal Y-type deposition and X and Z-type are characterized by $\phi = 0$ and $\phi = \infty$, respectively.

Summarizing, LB methods allow the deposition of very differently structured films and multilayers in a highly controlled manner. Although the method is limited to organic films the importance for applications in the field of information technology is increasing rapidly. Applications range from films for photolithography with improved homogeneity, flat-panel displays, optical devices, especially nonlinear optical devices, and finally the wide field of future molecular electronics [39].

5 Summary

In this short overview the methods used for the deposition of thin films from the materials of interest for information technology have been introduced. Even this selection of the most basic properties of the techniques should give an impression of the wide range of possibilities which are available. We have given special emphasis to deposition methods for metallic/magnetic films as considered for MRAM application and perovskite oxide films for DRAM, FeRAM, FeFET, conducting oxide electrodes and optical waveguides. Nevertheless it should be kept in mind that these deposition methods have also been developed to the highest precision for semiconductor films and especially superlattices, e.g. Si/Ge alloys and III-V compounds. In addition, these methods can be applied for organic films, and especially MBE and CVD are being considered for large-scale production of organic light-emitting diodes. All of these deposition methods have reached very high technical standards and the deposition of high-quality films for

most of the materials of interest can be achieved and has been achieved by several methods. Therefore, the optimum choice of method depends on details of the requirements and the differences between the requirements of research and production are often decisive. In addition to the properties listed in Table 1 we finally summarize some advantages and drawbacks of the methods.

MBE has been developed during the last 30 years to a high level of technical perfection and all components are commercially available. The method allows perfect layer by layer growth control and fairly independent control of the different deposit components and is therefore very flexible. Due to UHV conditions very clean films can be obtained and the method therefore is ideally suited for basic investigations of growth processes. For application as a production tool there are major drawbacks due to the generally rather slow layer by layer growth, the expensive UHV techniques and the large number of process parameters which have to be kept under control.

PLD is a well-developed thin film preparation method, and since the success of growing thin films from high temperature superconductors like YBaCuO the method has been shown to be especially suited for the deposition of oxides and other multicomponent materials. The PLD method offers several advantages compared to other deposition techniques, if the formation of multicomponent thin films is considered. The most important advantages of PLD are the stoichiometric transfer from a complex multi-elemental ceramic target material to the substrate without significant separation between the constituents and the rather high deposition rates. Therefore films can be optimized and deposited relatively fast. As the base vacuum is not critical for the process it may vary from UHV, e.g. for the additional option of in situ growth control, up to the oxygen partial pressures required for oxide growth. Disadvantages are the formation of droplets and boulders and the restriction to small substrate sizes, which can only be overcome by mechanical scanning of the substrates. For large-scale integration processes the low degree of conformal deposition is of concern.

Sputter deposition systems are well developed, commercially available and are standard techniques for metallization in CMOS production lines. Advantages are the large throughput, the large substrate sizes, good adhesion to the substrate due to the ion bombardment, often self-adjusting composition control, and less rigorous vacuum requirements than for thermal evaporation. The systems are very flexible and can be adjusted to many specific requirements. Additional modifications which could not be discussed here are e.g. bias sputtering in order to accelerate or decelerate the ions in a controlled manner, off-axis deposition in order to obtain more homogeneous deposition similar to PLD, and ion beam sputtering by the use of a controlled ion gun instead of the plasma as an ion source; as a further step of development multiple target systems, which are individually controlled, can be implemented. During sputtering of insulators there is a build-up of electrical load on the target which can be avoided by using an RF field; this RF field reduces the efficiency of the deposition and yields small deposition rates. Although only restricted conformality of the deposition can be achieved, this conformality is sufficient for many metallization requirements.

CVD techniques have been used for the deposition of thin films in many fields of modern technology and are standard processes in the CMOS technology for the deposition of insulators and interlayer dielectrics like SiO_2 and SiN_x and BPSG glasses. For the processing of many metals, however, special precursors in the form of organometallic compounds had to be developed in order to obtain a sufficient volatility and MOCVD emerged as a special subgroup of CVD techniques. MOCVD techniques are considered to be the primer deposition techniques in the field of high-K materials like $(Ba,Sr)TiO_3$ for advanced DRAM concepts as well as for ferroelectric materials like $Pb(Zr,Ti)O_3$) for ferroelectric memories due to their excellent film uniformity, compositional control, high deposition rates, and amenability to large wafer-size scaling. Moreover, the need for a high degree of film thickness conformality over the complex device topographies common to ULSI-scale circuits makes MOCVD one of the most appealing film synthesis methods. Limitations of the methods arise from the availability of suitable precursors, the very complex process parameter field and the very limited in situ control of the processes.

In addition to these depositions from the vapour phase we have included two examples of methods for deposition from solutions. The *advantages* of CSD are excellent control of the film composition through the stoichiometry of the coating solution, a relatively low capital investment, and easy fabrication over large areas, up to multiple square metres for dip and spray coating techniques. The *disadvantages* are some specific obstacles to achieving epitaxial films, the lack of an opportunity to deposit atomic layer superstructures, and poor step coverage for narrow submicron 3D structures.

LB methods are well-developed deposition techniques in surface chemistry and although the method is limited to organic films the importance for applications in the field of information technology is increasing rapidly. Applications range from films for photolithography with improved homogeneity, flat-panel displays, optical devices, especially nonlinear optical devices, and finally the wide field of future molecular electronics.

Finally, it should be mentioned that the borderlines between the methods are not sharp and there is some overlap. As the necessary components are commercially available even hybrid methods can easily be achieved, e.g. MOMBE or a combination of thermal evaporation with simultaneous ion bombardment, ion-beam-assisted deposition, IBAD. Nevertheless, every new material and especially every new material combination presents a new challenge, and new ideas, like the recent applications of SURFACTANT's, and also very detailed optimization of the processes are necessary.

Acknowledgements

The editor would like to thank Sam Schmitz (CAESAR, Bonn) for checking the symbols and formulas in this chapter.

References

[1] R.F. Bunshah, *Handbook of Deposition Technologies for Films and Coatings*, Noyes Publ., Park Ridge, 1994.

[2] K.L. Chopra, *Thin Film Phenomena*, McGraw-Hill, NY, 1969.

[3] J.Y. Tsao, *Materials and Fundamentals of Molecular Beam Epitaxy*, Acad. Press, SanDiego, 1993.

[4] R.H. Lamoreaux, D.L. Hildenbrand, and L.Brewer, J. Phys. Chem. Ref. Data **16**, 419 (1987).

[5] B. Voigtländer, Experimente zum epitaktischen Wachstum, 28. Ferienkurs des FZ-Juelich, p.C3.1 (1997).

[6] E.H.C. Parker, (ed.), *The Technology and Physics of Molecular Beam Epitaxy*, Plenum Press, New York, 1985.

[7] M.A. Herman und H. Sitter, *Molecular Beam Epitaxy*, Springer Series in Materials Science, 2. Edition, 1996.

[8] P. Berberich, W. Assmann, W. Prusseit, B. Utz, H. Kinder, J. of Alloys&Compounds **195**, 271 1993.

[9] J.A. Stroscio, D.T. Pierce, and R.A. Dragoset, Phys. Rev. Lett. **70**, 3615 (1993).

[10] O. Auciello, A.I. Kingon, A.R. Krauss and D.J. Lichtenwalner, in *Multicomponent and Multilayerd Thin Films for Advanced Microtechnologies: Techniques, Fundamentals and Devices*, O. Auciello and J. Engemann, eds., Kluwer Acad.Press, 1993. p. 151 – 208

[11] D.B. Chrisey and G.K. Hubler, (eds.), *Pulsed Laser Deposition of thin Films*, John Wiley & Sons, NewYork, 1994.

[12] B. Holzapfel, B. Roas, L. Schultz, P. Bauer, G. Saemann-Ischenko, Appl. Phys. Lett. **61**, 3178 (1992).

[13] M. Siegert, J.G. Lisoni, C.H. Lei, A. Eckau, W. Zander, J. Schubert, and Ch. Buchal, Mat. Res. Soc. Proc. **597** 145 (2000).

[14] S.M. Rossnagel, in [10] p.1-20.

[15] K. Wasa and S. Hayakawa, *Handbook of Sputter Deposition Technology: Principles and Applications*, Noyes, Park Ridge, 1992.

[16] G.K. Wehner and G.S. Anderson, in *Handbook of Thin Film Technology*, L.I. Maissel and R. Glang, eds., McGraw-Hill, NY, 1970. p. 3.1 – 3.38

[17] J.A. Thornton, J. Vac. Sci. Technol. **11**, 666 (1974).

[18] U. Poppe, N. Klein, U. Dähne, H. Soltner, C.L. Jia, B. Kabius, K. Urban, A. Lubig, K. Schmidt, S. Hensen, S. Orbach, G. Müller, and H. Piel, J. Appl. Phys. **71**, 5572 (1992).

[19] U. Poppe, R. Hojczyk, C.L. Jia, M.I. Faley, W. Evers, F. Bobba, K. Urban, C. Horstmann, R. Dittmann, U. Breuer, H. Holzbrecher, IEEE Transaction on Appl. Supercond., **9**, 3452 (1999).

[20] M.L Hitchman. and K.F., Jensen, *Chemical Vapor Deposition, Principles and Applications*, Academic Press, 1993.

[21] H.O. Pierson, *Handbook of Chemical Vapor Deposition, Principles, Technology and Applications*, Noyes Publ. Park Ridge, NJ, 2nd ed. 1999.

[22] C.E Morosanu, *Thin Films by Chemical Vapor Deposition*, Elsevier, Amsterdam-Oxford-New York-Tokyo, 1990.

[23] R. Waser, T. Schneller, S. Hoffmann-Eifert, P. Ehrhart, Integrated Ferroelectrics **36**, 3 (2001).

[24] F. Felten, J.-P. Senateur, F. Weiss, R. Madar, and A. Abrutis, Journal de Physique, IV, C5-1079 (1995)

[25] C.M. Foster, in: *Thin Film Ferroelectric Materials and Devices*, R. Ramesh, ed., Kluwer Acad.Publ., Boston, 1997. p. 167 – 197

[26] C.S. Kang, H.-J. Cho, C.S. Hwang, B.T. Lee, K.-H. Lee, H. Horii, W. D. Kim, S. I. Lee , and M.Y. Lee., Jpn. J. Appl. Phys. **36**, 6946 (1997).

[27] P. Ehrhart, F. Fitsilis, S. Regnery, C.L. Jia, H.Z. Jin, R. Waser, F. Schienle, M. Schumacher, and H. Juergensen, Mat. Res. Soc. Proc. **655**, CC9.4.1 (2001).

[28] J.H. Han, H.-K. Ryu, C.-H. Chung, B.-G. Yu, and S.H. Moon, J. Electrochem. Soc. **142**, 3980 (1995).

[29] S.R. Summerfelt in [25], p.1-42.

[30] C.S. Hwang, J. Park, D.S. Hwang, and C.Y. Yoo, J. of the Electrochemical Soc. **148**, G636 (2001) and private communication.

[31] M. Leskelä and M. Ritala, J. de Physique **IV**, C5 –937 (1995).

[32] M. Vehkamäki, T. Hatanpää, T. Hänninen, M. Ritala, and M. Leskelä, Electrochem. and Solid-State Lett. **2**, 504 (1999).

[33] R.W. Schwartz, Chemistry of Materials **9**, 2325 (1997).

[34] T.M. Lu, S.P. Murarka, T.-S. Kuan, and C.H. Ting (eds.), *Low-Dielektric Constant Materials – Synthesis and Applications in Microelectronics*, Mat. Res. Soc. Symp. Proceed. **381** (1995).

[35] D.E. Hooks, T. Fritz, and M.D. Ward, Adv. Mater. **13**, 227 (2001).

[36] G. Gu, G. Parthasarathy, and S.R. Forrest, Appl. Phys. Lett. **74**, 305 (1999).

[37] G. Roberts, (ed.), *Langmuir-Blodgett Films*, Plenum Press New York, 1990.

[38] A. Ulman, *An Introduction to Ultrathin Organic Films, from Langmuir Blodgett to Self-Assembling*, Academic Press, Boston, 1991.

[39] A. Ulman, (ed.), *Organic Thin Films and Surfaces: Directions for the Nineties*; Thin Films, **20**, Acad Press, Boston, 1995.